Available online at www.sciencedirect.com
ScienceDirect
Journal of Power Sources 176 (2008) 499–514
JOURNAL OF POWER SOURCES
www.elsevier.com/locate/jpowsour

The development of a small PEMFC combined heat and power system

Hsin-Sen Chu, Fanghei Tsau *, Yi-Yie Yan, Kan-Lin Hsueh, Fa-Lin Chen

Energy and Environment Research Laboratories, Industrial Technology Research Institute, No. 195 Section 4 Chung-Hsing Road, Chutung, Hsinchu 310, Taiwan, ROC

Available online 2 September 2007

Abstract

A proton exchange membrane fuel cell combined heat and power system has been chosen as a platform on which key components and system integration technologies have been developed to advance the applications of fuel-cell technology. The prototype system consists mainly of a fuel-cell stack, a natural gas reformer to supply hydrogen-rich reformate gas to the stack, a power conditioner to convert and invert the electricity generated by the stack, and a water and heat management network to provide the oxidizer (air) to and necessary cooling and humidification for the stack. The design of the stack and its components, catalysts development, design and testing of the natural gas reformer, were studied. In addition, the durability of a CO tolerant membrane-electrode-assembly has been studied with the assistance of air bleeding. Preliminary testing of the prototype combined heat and power system was carried out. It was found that the maintenance of a uniform output voltage across all single cells was more difficult with reformatted gas rather than using pure hydrogen. It was also found that the design of water and heat management network played an important role in the overall efficiency of the system.

Keywords: Combined heat and power system; Natural gas reformer; System integration; Proton exchange membrane fuel cell

1. Introduction

Several types of fuel cells are in various stages of development and applications [1–3]. For example, both alkaline and phosphoric acid fuel cells have been in space and field services for quite some time. However, the limitations on the environment in which the alkaline fuel cell can operate durably and the high cost per unit power output and of maintenance have restricted the mass deployment of the two fuel cells. Molten carbonate and solid oxide fuel cells are high-temperature fuel cells more suitable for attended stationary applications. Many molten carbonate fuel cell systems are undergoing field trials presently. Proton exchange membrane and direct methanol fuel cells (PEMFC and DMFC) are attracting lots of attention nowadays due to their low-temperature operation, which makes them suitable for unattended stationary, transportation and mobile applications. The technologies are quite advanced and there is a potential for significant cost reduction. They are often referred together as polymer electrolyte membrane (PEM) fuel cells because both use proton-conducting polymers as solid electrolyte. PEM fuel cells have made great progress for the last 5–10 years. Up to 2004, more than 80% of the prototype fuel-cell systems announced were PEM fuel cells, PEMFC for stationary and transportation and DMFC for mobile applications [4,5].

Much of the R&D activities on PEMFC have been focused on the fuel-cell stack and in particular on the proton transport media [6]. A functional and practical PEMFC is a system, which consists of at least a fuel supply, an oxidizer (air) supply and water, heat management sub-systems in addition to the fuel-cell stack [7,8]. The system very likely includes also a power conditioner to supply the electricity as per the specifications of the required application. The fuel supply sub-system can range from just a simple source of pure hydrogen to a reformer which converts hydrocarbon fuels to a reformate gas-rich in hydrogen. For instance, if the primary fuel is natural gas (methane), the natural gas is converted into a reformate gas of hydrogen (40–80%, v/v), carbon dioxide, carbon monoxides and trace level of other impurities. In fact, this reformates gas from hydrocarbons will

Abbreviations: APDL, ANSYS parametric design language; ATR, autothermal reforming; CHP, combined heat and power; GDL, gas diffusion layer; DMFC, direct methanol fuel cell; DOE, Department of Energy; FEM, finite element analysis; GHSV, gas hourly space velocity; LPG, liquid propane gas; NG, natural gas; MEA, membrane electrode assembly; MPL, micro-porous layer; PEM, proton exchange membrane; PEMFC, proton exchange membrane fuel cell; PrOX, preferential oxidation reaction; PTFE, poly tetra-fluoroethylene; PWM, pulse width modulation; SLPM, standard liter per minute; SRG, simulated reformate gas; THD, total harmonic distortion; WGS, water–gas shift reaction.

* Corresponding author. Tel.: +886 591 5394; fax: +886 582 0230.
E-mail address: Fanghei@itri.org.tw (F. Tsau).

0378-7753/$ – see front matter © 2007 Elsevier B.V. All rights reserved.
doi:10.1016/j.jpowsour.2007.08.072

Nomenclature

D	manifold width (mm)
E_r	reversible cell voltage (V)
i_o	exchanging current density of oxygen reduction ($A\,cm^{-2}$)
i_{loss}	current loss due to hydrogen crossover ($A\,cm^{-2}$)
I_L	mass transfer limiting current density ($A\,cm^{-2}$)
R_i	cell internal resistance (Ω)

Greek letters

η_{act}	activation over-potential (V)
η_{conc}	concentration over-potential (V)
η_{ohm}	ohmic over-potential (V)
η_{xover}	hydrogen crossover over-potential (V)
κ	permeability

probably be the main form of hydrogen energy in the foreseeable future except for the transportation application where pure hydrogen will be required. The gas mixture is fed to the fuel-cell stack where through electrochemical reactions electricity and heat are produced with water as by-product. Not only must the heat and water be removed from the fuel-cell stack, but also the remainder of the reformate gas (also called tail gas) must be exhausted from the fuel-cell stack. This latter feature of employing a reformate gas and handling the tail gas sets the design of the fuel-cell stack and the system apart from those consuming pure hydrogen as fuel [8–10].

The major reason to embrace fuel-cell technologies is the expected overall energy conversion efficiency, electrical plus thermal efficiency. This is especially the case for stationary applications if hydrocarbons are the primary fuels or hydrogen is derived from hydrocarbons. A simple estimate for a low-temperature PEMFC CHP system from the reformer to the stack would reveal that the electrical efficiency is approximately maximized around 30–35%. Taking into account parasitic consumptions would only decrease the efficiency and make it closer to the efficiency with which we normally receive power from the grid [9–11]. In other words, the thermal energy utilization, roughly 1.5–2.0 times the electrical energy, is the key to actual efficiency gain and hence the system integration. In practical circumstances, the electrical and thermal demand patterns and their ratios at any given interval may vary. Hence, variable heat-to-power control strategies [8] at the expense of more system complexities, cost and/or sizing are necessary to maintain the efficiency gain. Durability is another major technical issue [12], which is mainly linked with the reformer operation [10]. The preferential oxidation (PrOX) reaction which control the carbon monoxide level in the reformate is highly sensitive to temperature [13]. Higher carbon monoxide level in the reformate will definitely affect the durability of the stack.

Fig. 1 shows the schematic diagram of the PEMFC CHP system under development. The reformer (fuel processor) is an auto-thermal one designed to shorten the start-up time. It can work on both natural gas (NG) as well as liquid propane gas (LPG) as fuels. The reformate gas after preferential oxidation will contain mainly hydrogen, nitrogen, carbon dioxide, carbon monoxide and traces of unconverted fuels. This mixture of gases is fed to the anode of the fuel-cell stack and the energy of the tail gas is recovered via catalytic combustion. As carbon monoxide concentration can be varying during practical operations, CO-poisoning endurance is an important design requirement that may not be met fully by just anode catalysts design. Filtered air is supplied to the cathode of the fuel-cell

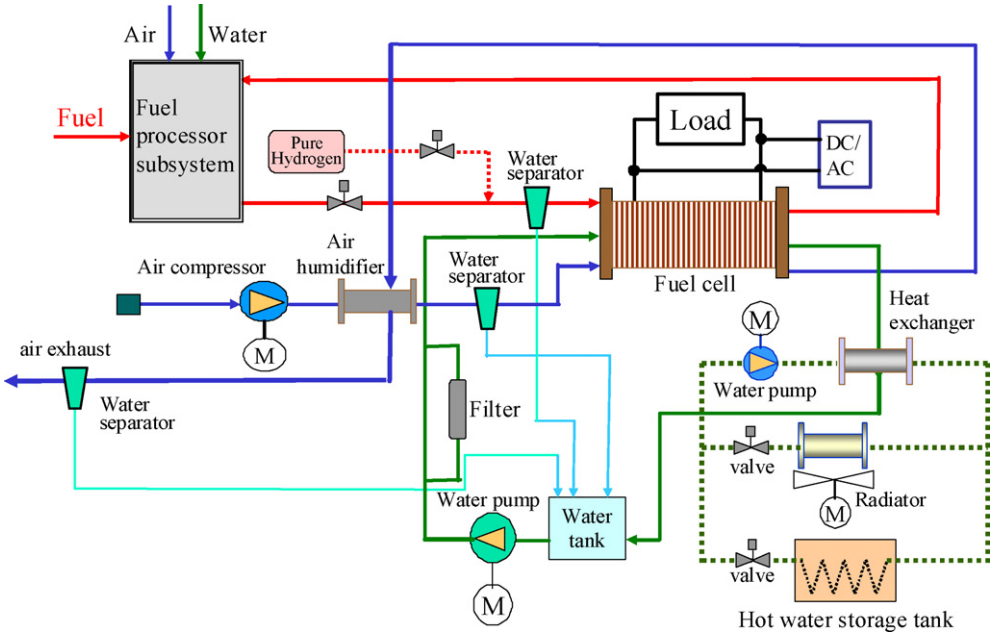

Fig. 1. The schematic diagram of the PEMFC CHP system under development.

stack and the exhaust after reaction is past through a passive air humidifier to increase the humidity of and pre-heat the incoming cathode air stream. Heat generated by the fuel-cell stack is recovered by circulating cooling water through the stack. Thermal energy is further exchanged down stream with the second water loop for heating water purpose. If necessary, a radiator is also used for temperature control. Excessive water in the system is recovered to the extent possible to conserve water usage as well. Electricity generated by the stack is conditioned by a set of power electronics to be consumed internally, to supply electricity to external specifications and to charge the start-up battery (not shown in the figure). The progress made in the development of a combined CHP system including the components and the preliminary test results are presented in the following sections.

2. Brief description of the small PEMFC CHP system

The entire power system was placed inside a chase with the dimensions of 1.2 m × 0.7 m × 1.40 m. It includes a 250 L hot water tank, fuel-cell stack, and sub-systems of fuel and air supply, water cooling, heat recovery, sensing and controlling, and power conditioning. The system was capable of delivering 110 V/60 Hz ac power and 60 °C hot water.

This system used pipeline natural gas as its fuel. It could also by-pass the reformer and use pure hydrogen as the fuel. Flow diagram of this CHP power system is shown in Fig. 1. Fuel processing subsystem is an auto-thermal reformer, which converts natural gas into a hydrogen-rich gas. The reformer included an auto-thermal reformation, water–gas shift, and 1–3 stages of preferential oxidation sections. Start-up time of this reformer was about 30 min and hydrogen concentration in the exit gas was about 45%. Hydrogen flow rate was higher than 50 L min^{-1}. The methane conversion rate was greater than 95% and carbon monoxide concentration was less than 10 ppm.

Air for the cathode was warmed up and humidified by passing through an air humidifier (Fig. 1) before entering the cathode chamber. The structure of air humidifier was similar to a tube-shell heat exchanger. The tubes were bank of hollow Nafion tubes. Fresh air was fed inside the tubes, warm and humid air from the cathode outlet was fed outside the tubes. Heat and moisture exchange happened on the walls of the hollow Nafion tubes.

Heat from the stack was removed by the cooling water circulating loop. A brazed plate heat exchanger recovered heat from the cooling water and transferred to the water tank. Temperature of the water tank was kept at 60 °C max, and a radiator was used to disperse the excess heat. The above heat-recovering scheme increased the overall energy efficiency of the power system.

Power conditioning unit (dc/ac in Fig. 1) included a dc/dc converter and a dc/ac inverter. dc/dc converter converted a portion of the power generated by the stack into a 24 V dc for system balance of plant (BOP) needs. dc/ac inverter converted the majority of the dc power into 110/220 V 60 Hz ac power for general applications.

3. Status of development

3.1. Reformer

Reformer is a necessary subsystem of the PEMFC co-generation system that is to be utilized without concern for the hydrogen supply infrastructure. The function of a reformer is to transforms hydrocarbons into a hydrogen-rich gas containing CO concentration less than 10 ppm. In contrast to a fuel-cell stack, the control strategy for the reformer is more complicated and the stability and reliability of the reformer is very important. In order to develop the small PEMFC co-generation system, a NG/LPG reformer is developed using auto-thermal reforming technology. The reformer consists of auto-thermal reforming (ATR), water–gas shift reaction (WGS), CO preferential oxidation, and catalytic oxidation of the anode exhaust gas sections. The reformer developed emphasizes compactness, short start-up time, and low-precious metal loading. In addition, the catalysts used for the reformer are precious metal-based and they are developed in-house.

NG and LPG are the most common fuels for residential usage in Taiwan. The Ru or Rh containing catalysts are extensively used for NG reforming. However, the LPG will have some quantity of olefin, which might result into coking on ATR catalyst surface. Although increasing steam-to-carbon molar ratio can lessen coking phenomena, thermal efficiency of the reformer may be compromised. Therefore, a Rh–M catalyst is developed to prevent the coking problem in the reformation section.

In the WGS reaction, the reformate gas mixture having about 3.0% CO is reacted with steam to produce CO_2 and H_2. From the thermodynamic point of view, lower reaction temperature favors reduction of CO concentration. The catalyst normally used for WGS reaction in the petroleum industry is Cu–Zn/Al_2O_3. The catalyst must be kept in an inert atmosphere. It has to be activated in situ and the gas hourly space velocity (GHSV) is low. Hence, it is not a suitable catalyst for the miniaturization development of a reformer. There are continuing efforts in trying to develop more active and robust WGS catalysts [14–16]. The performance of a Pellet and honeycomb type Pt-based WGS catalysts developed is shown in Figs. 2 and 3. The monolithic catalyst exhibits higher CO conversion and lower reaction temperature than a commercial Pt-based catalyst (Pt loading 2 wt.%) under the same reaction conditions, H_2 50%, CO 8%, steam/CO = 6 molar ratio, and GHSV 6000 h^{-1}. The pellet catalyst exhibits higher activity due to lower reaction temperature (250 °C) and the CO conversion on the pellet catalyst (87%) is higher than that on Cu–Zn/Al_2O_3 (70%) under the low-CO concentration condition: H_2 50%, CO 4%, steam/CO = 6 molar ratio, GHSV 5000 h^{-1}, and 250 °C.

PrOX reaction is a critical stage to ensure CO concentration in the reformed gas is lower than 10 ppm, which is considered the maximum CO level safe for the stack operation. In order to enhance CO conversion or selectivity of the catalyst, major control parameters are the O_2/CO molar ratio, GHSV velocity, CO inlet concentration, steam concentration and catalyst type. From our experience, the catalyst is very crucial for PrOX reaction. Pt/zeolite, Pt/Al_2O_3 and Ru/Al_2O_3 are often mentioned for the

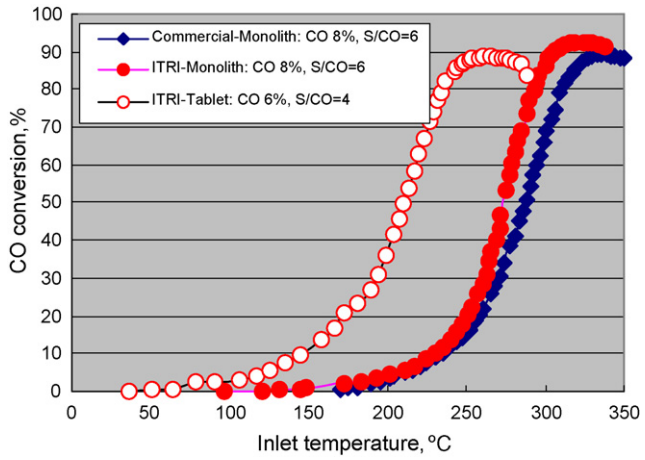

Fig. 2. Performance of in-house developed and commercial catalyst for WGS reaction (reaction conditions: H_2 50%, CO 6–8%, $H_2O/CO = 4–6$; GHSV = 6000 h^{-1}).

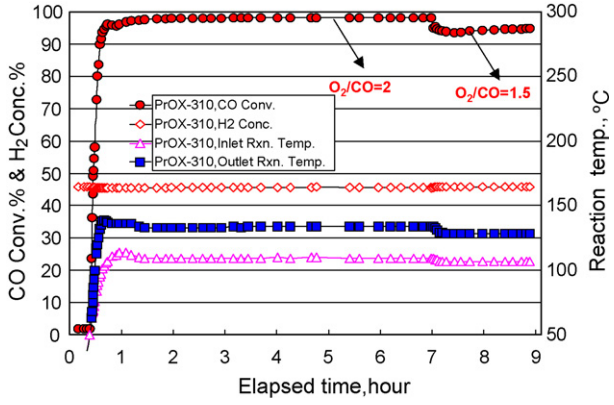

Fig. 3. Performance of in-house catalyst for PrOX reaction (reaction conditions: H_2 50%, CO 0.6%, $O_2/CO = 1.5–2$, H_2O 26%; GHSV = 13,500 h^{-1}).

PrOX reaction. In addition, the steam concentration also affects the performance and durability of the catalyst. Fig. 3 displays the performance of the catalyst under reaction condition: H_2 50%, CO 0.6%, $O_2/CO = 2$ molar ratio, H_2O 26%, and GHSV 13500 h^{-1}. Under this high-steam concentration condition, CO conversion on catalyst is close to 98%. If O_2/CO molar ratio is reduced to 1.5, CO conversion on catalyst is slightly reduced to 95%. The catalyst for PrOX reaction has been tested for more than 300 h.

The reformer consists of ATR, WGS, several stages of PrOX reaction, and tail gas oxidation. The dimension of the main system is height 70 cm, width 40 cm and depth 25 cm. Performance of the reformer using LPG as the feed is given in Fig. 4a. The temperatures of ATR, WGS, and PrOX were at 400, 320, and 150 °C, respectively. The reformer was operated under the following operating conditions: O_2/LPG molar ratio 1.2, water/LPG molar ratio 6. Start-up time of the reformer was around 30 min. The reformed gas had hydrogen concentration of ~43% (in dry) and CO concentration less than 15 ppm. The hydrogen production rate was around 45 L min^{-1} (NTP) and LPG conversion efficiency was higher than 95%. Performance of the reformer using natural gas feed is given in Fig. 4b. In this case, temperature of ATR, WGS, and PrOX were 500, 320, and 150 °C, respectively. The reformer operating conditions are O_2/C molar ratio 0.47, water/C molar ratio 2.4. The start-up time was around 25 min. The reformed gas has about 50% (in dry) hydrogen and CO less than 20 ppm. The hydrogen production rate is about 60 L min^{-1} and natural gas conversion is close to 95%. The thermal efficiency of NG reformer is about 73% (HHV) and the precious metal usage of this reformer is roughly 6–7 g kW^{-1}.

3.2. Power conditioning unit

Fuel cell has been considered as an ideal source for the auxiliary power unit or ultra-clean residential power source. Normally, fuel cell systems can couple with standalone or grid-tied power conditioners as shown in Fig. 5. As shown in Fig. 5a, on either lower dc side or higher dc side of standalone type application needs some storage system to prevent the output power loss of fuel cell. Grid-tied application does not need such storage systems, but it should consider the power island situation. The output voltage range of fuel cell depends on the number of cells stacked in series. The nominal output voltage is set at 48 V, which is not suitable for directly supplying of power to either telecommunication or residential applications.

When supplying the utility type ac output, the main issue of converter is low-dc output voltage from fuel cell and high ac output voltage required for applications. In order to generating 50/60 Hz, 110/220 V ac voltage for residential applications from

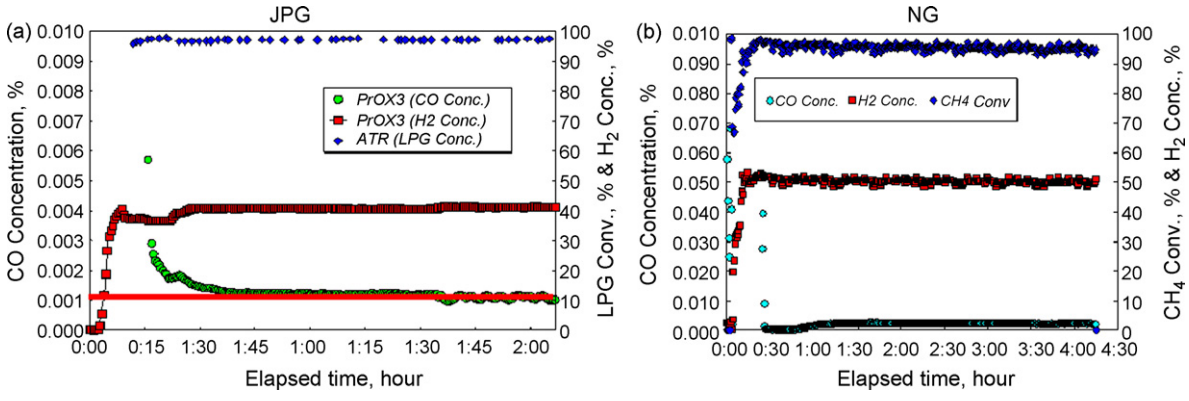

Fig. 4. The performance of ITRI's NG/LPG reformer systems.

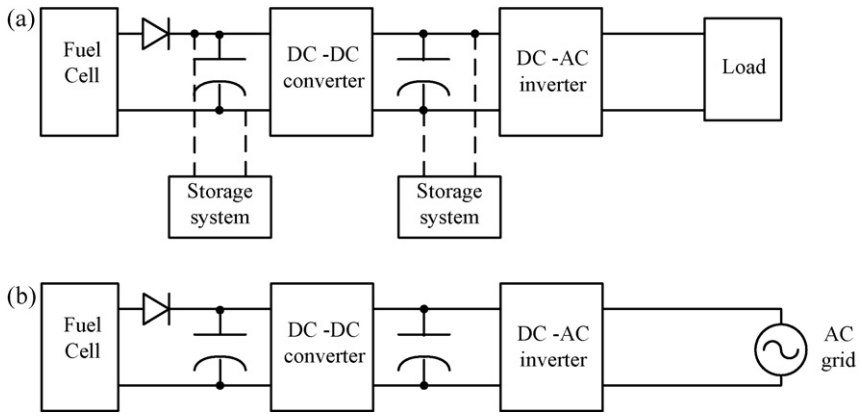

Fig. 5. Block diagram of the fuel-cell power conditioner system: (a) standalone type power conditioner and (b) grid-tied power conditioner.

Table 1
Specifications of power conditioner

Item	Specification
Output	
Connection	Single phase, two wire
Voltage THD	<5% typical for linear loads
Voltage	110 Vac, 60 Hz
Power rating	4 kVA/3 kW Max
Fuel-cell input	
Input voltage range	40–70 Vdc
Nominal input voltage	48 Vdc

low-output dc voltage fuel cell system, a large current capacity dc–dc converter is required to boost the fuel cell low output dc voltage to high-voltage level, which then can be converted to the desired ac output through a dc–ac inverter. For 110 and 220 V ac output, the dc voltages of the dc–dc converter output or the dc–ac inverter input are typically 200 and 400 V, respectively.

The specification of the PEMFC power conditioner is shown in Table 1. There are many kinds of converter topologies with isolation and high-boost ratio, such as forward, push-pull, half bridge and full bridge circuits [17]. In the front-end dc–dc converter, the voltage drop of power devices due to high-power current would be very significant for efficiency improvement. Thus parallel conversion power devices with low-voltage rating and low on-resistance can reduce the devices loss and ensure reasonable power conversion efficiency. Considering the output current ripple, cost, and efficiency of fuel cell power conditioner, we choose a topology of multi-phase/interleaved dc–dc converter and a full bridge construction for dc–ac inverter. In dc–ac inverter, the unipolar pulse width modulation (PWM) [18] switching technique is used to reduce the switching loss of inverter and to reduce the size of output filter inductors. Synchronizing the switching between dc–dc converter and dc–ac inverter reduces the ripple voltage of the intermediate dc bus (Vdc).

The measured waveform of inverter output is shown in Fig. 6. The total efficiency of power conditioner is around 85% at fuel cell output voltage of 50 V. The total power conversion efficiency and the distortion of output voltage waveform are acceptable. The efficiency losses of power conditioner are mainly due to the conduction and switching losses in dc–dc converter, the transformer loss, the parasitic resistors loss of PCB patterns, and connection wires. To improve the power conversion efficiency, we need new devices, new magnetic material for transformer, and new construction of circuit. Moreover, new control strategy is necessary to improve the output voltage waveform and reduce the total harmonic distortion (THD).

3.3. Stack

A uniform distribution of gases and their flow field is essential to have good utilization of individual cell of a stack. It also

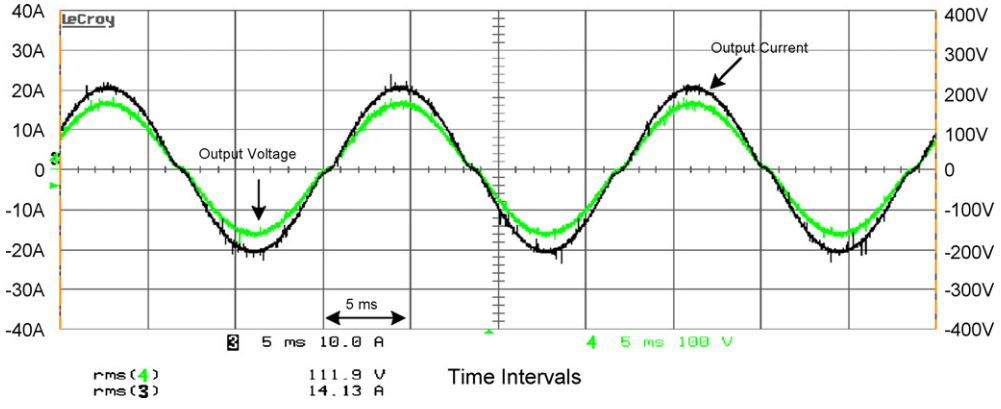

Fig. 6. Fuel-cell power conditioner output waveform on resistor load.

avoids possible hot spot and local starvation of reactants. We have developed a computational fluid dynamic-based model for gas manifold design. The other mechanical issue of the stack is uniformity of clamping force from the end plates. An uneven distribution of the clamping force not only causes crack of the fragile bipolar plate but also causes leakage of gas from the sealing. We use a commercial package to analyze the stress of each component within the stack. This analysis results a new stack design.

The main components of a stack are the MEA, bipolar plate, and gas sealing. Conventional bipolar plate is made of graphite and flow channels on the plate needs extensive machinery work. The material cost and labor cost make bipolar plate very expensive and is one of the major costs of fuel-cell stack. We use composite material with injection molding process for the bipolar plate. This composite bipolar plate significantly reduces machining cost and time. The material cost is also reduced. MEA is the key component that determines output power density and conversion efficiency of the stack. Its CO tolerant level decides the requirement of reformer. Since MEA used for stack are purchased from commercial supplier, we need to know the MEA behavior for quality control as well as for system design purposes.

An MEA includes gas diffusion layer, catalyst layer, and the proton exchange membrane. The hydro-phobicity, porosity, and thickness of the micro-porous layer on the GDL affect the MEA performance and its water management. A preliminary study is conducted to evaluate the MEA performance at different concentration of PTFE in the GDL and in the MPL. A summary of the study is presented in the following subsections.

3.3.1. MEA performance and breakdown of voltage losses

To have a better understanding of the MEA used in the stack, we test single cell in parallel with the stack. A commercial MEA was used in the single cell as well as fabrication of the stack. The membrane used in this MEA has a composite structure. The membrane is made of an expanded mesh of poly tetra-fluoroethylene (PTFE). The pores in the membrane matrix are filled with proton conducting fluoro-polymer. The expanded mesh structure enables thinner membrane with enhanced mechanical properties. The membrane has better conductivity and voltage loss due to ohmic resistance is minimized.

Several factors are responsible for the fuel cell voltage loss. They are hydrogen crossover over-potential loss (η_{xover}), catalyst activation over-potential loss (η_{act}), internal ohmic over-potential loss (η_{ohm}), and concentration over-potential loss (η_{conc}). These over-potential losses can be separated by using a semi-empirical equation. The voltage losses due to various over-potentials can be determined by fitting the equation with the measured voltage–current data. Many semi-empirical equations are proposed in the literature [19–23] for the same purpose. However, hydrogen cross over is not considered in those equations. We feel that this factor cannot be ignored and shall be taken into consideration. In our approach, a similar equation with additional over-potential of hydrogen crossover is constructed

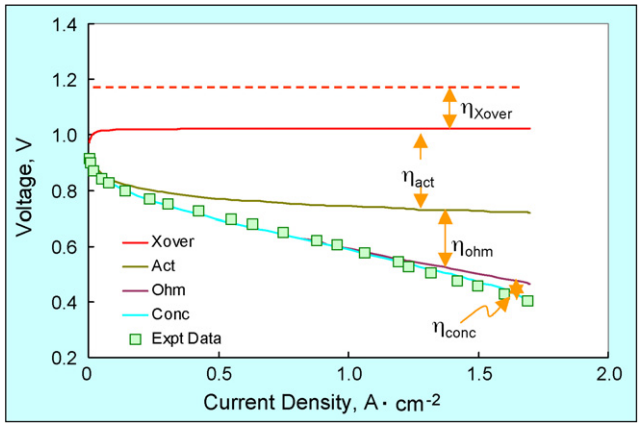

Fig. 7. Break down of voltage losses. Test conditions of this experiment are the following: MEA active area at 25 cm^2 (5 cm × 5 cm), anode gas of H_2 and cathode gas of air at 34.5 kPa, cell temperature at 65 °C, H_2/air humidification at saturation, H_2/air flow rate at 1.5×/3.0× stoichiometry and H_2 pressure ambient.

as shown below

$$E = E_r - \eta_{xover} - \eta_{act} - \eta_{ohm} - \eta_{conc} = E_r - \frac{RT}{\alpha F}\ln\left(\frac{i + i_{loss}}{i_o}\right) - \frac{RT}{\alpha F}\ln\left(\frac{i}{i_o}\right) - R_i i - \frac{RT}{nF}\ln\left(\frac{i}{i_L - i}\right) \quad (1)$$

Here i_{loss} is the current loss due to hydrogen crossover, i_o the exchanging current density of oxygen reduction, R_i the internal resistance of the cell and i_L is the mass transfer limiting current density of oxygen at the cathode. Breakdown of a typical current voltage curve into various over-potential losses is depicted in Fig. 7. The cell was operated at 65 °C with air pressure at 34 kPa, hydrogen at ambient pressure and stoichiometry of hydrogen/air is 1.5/3.0. It can be seen from the figure that at the current density of 1 A cm^{-2}, the output cell voltage is 0.6 V. This corresponds to an efficiency of only 48% (0.6/1.23) with the voltage loss of 0.63 V. About 50% (0.3/0.63) of the voltage loss is due to the catalyst activation loss (η_{act}) and another 30% (0.2/0.63) is due to internal resistance (η_{ohm}). The voltage loss due to mass transfer is not significant.

The carbon monoxide present in the reformate gas may preferentially adsorb onto the Pt catalyst surface thus poisoning it. The anode catalyst poisoning may result in the loss of fuel cell performance. Various strategies like the use of alloy catalysts, high-temperature operation, and air bleeding are being studied to circumvent the CO poisoning problem. In the air bleeding process, CO adsorbed on the catalyst surface can be desorbed by converting to carbon dioxide (CO_2). The effect of air bleeding on the performance of a fuel cell operated at 0.60 V with 52.7 ppm of CO in the hydrogen feed is given in Fig. 8. Bleeding the anode hydrogen stream with 2% and 4% air improves the current density from 0.2 to 0.75 A cm^{-2} and 1.5 A cm^{-2}, respectively. Air concentration higher than 4% has little effect on the current density. The results show the 4% air bleeding can re-activate the catalyst within 10 min.

In order to investigate the long-term effect of reformate gas on the performance of MEA, a 5 cm × 5 cm test cell was operated

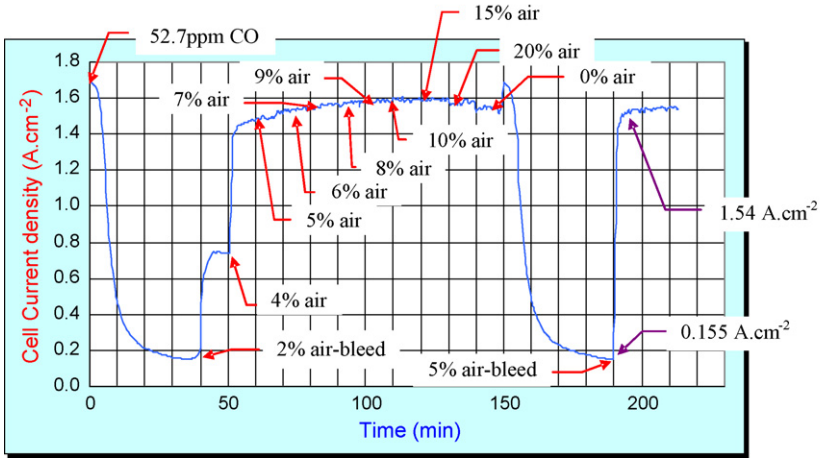

Fig. 8. Effects of injecting air concentration on cell discharge current density. Experiment was carried out at cell temperature 65 °C, H_2/O_2 humidification temperature 80/70 °C, H_2/O_2 stoichiometry ratio 1.5×/2×, ambient pressure and CO concentration of 52.7 ppm.

using simulated reformatted gas (SRG) for 3068 h. The SRG has the composition of hydrogen, nitrogen, and small amount of CO. This gas is gradually poison catalyst inside MEA and reduces its output power. It is important to know the effects of CO on MEA long-term performance. Single cell is used for long-term constant current discharge experiment. The active area of the MEA tested is 5 cm × 5 cm. The cell temperature is kept at 55 °C. Experiment was carried out at 0.3 mA cm^{-2} constant discharge current density. Air was fed into the cathode and CO contained hydrogen was fed into the anode to SRG. Gas SRG/air is 1.5/2.9 stoichiometry flow ratio. The open circuit voltage was 0.94 and was 0.69 V at 0.3 A cm^{-2}. After 3068 h discharging, the cell voltage was decreased from 0.69 to 0.64 V. Voltage degradation rate was 2.86% (3068 h) and average cell voltage was 0.67 V.

3.3.2. Gas diffusion layer

The main functions of GDL in the MEA are to conduct electric current and to distribute the gaseous reactants evenly to the catalyst layer. In addition to the above functions, hydrophobicity and porosity of GDL/MPL play an important role in the maintenance of sufficient water balance within MEA. The optimum water balance is very important for the performance of MEA and membrane conductivity [24–26]. The optimal composition and structure of the GDL and MPL is depending on the MEA characteristics (such as catalyst activity, porosity, and hydrophobic) and system operating conditions (such as humidity, flow rate, and temperature). Present study is to search the optimal GDL/MPL composition and structure of the MEA used in stack.

The GDL consists of a carbon fiber layer and micro-porous layer. The carbon fiber layer can be either carbon cloth or carbon paper treated with PTFE. The average pore size of this layer is in the order of 1–50 μm. The MPL is made of carbon powder having the particle size of 50 nm and PTFE as the binding agent. Average pore size of this layer is in the range of 0.05–0.5 μm.

The effect of PTFE content in the GDL/MPL layer on the performance of the single cell is evaluated to identify the optimum conditions of GDL/MPL. The substrate is Toray carbon paper (Toray, TGP-H-090). Commercial MEA was used with active area of 25 cm^2, anode catalyst loading was 0.45 Pt–Ru mg cm^{-2} and cathode catalyst loading was 0.6 Pt mg cm^{-2}. The thickness of polymer membrane was 35 μm. The PTFE suspension from Du Pont was used as the binding agent for MPL as well as hydrophobic material for the GDL. Carbon powder Vulcan XC-72R was used for the formation of MPL layer. The POCO graphite (AXF-5QCF) bipolar plates were used in the studies. Pure H_2 and O_2 were used as the anodic, cathodic fuel. The stochiometric ratios of anode/cathode gas were 1.5×/2.0×, respectively at ambient pressure. The gases were humidified by bubbling through a water bottle. The humidification temperature for cathode and anode were kept at 70 and 80 °C, respectively. Cell temperature was maintained at 65 °C. The in-house test station with an electronic load from Agilent (Agilent 6060B) was used for this purpose.

The performance of MEA with and without the MPL layer was investigated. The single cell performance for various concentrations of PTFE in the GDL (without MPL) is given in Fig. 9a. High content of PTFE makes the GDL more hydrophobic, which will reduce cathode flooding and improve oxygen mass transfer to the cathode. However, very high-PTFE loading will increase the electrical resistance of GDL and block the gaseous mass transfer. Hence, the GDL with 10% PTFE has the highest performance among others. The performance of MEAs with MPL having different amount of PTFE where all the carbon papers contained 10% PTFE are presented in Fig. 9b. It can be seen from the results that the MPL with 20% PTFE loading had the highest performance. The PTFE treatment of the GDL and MPL significantly increases the mass transfer limiting current density. The best combination of PTFE loading is 10% for GDL and 20% for MPL. With this PTFE composition in the GDL/MPL, the current density at 0.6 V cell voltage reaches 2 and 0.9 A cm^{-2} with oxygen and air, respectively.

3.3.3. Bipolar plate

Bipolar plates make up most of the volume, weight and cost of the PEMFC stack. Hence, the development of new bipolar plate materials is very important for the advancement of the PEMFC technology. The bipolar plates serve multiple functions in the operation, such as distributing reactant gases

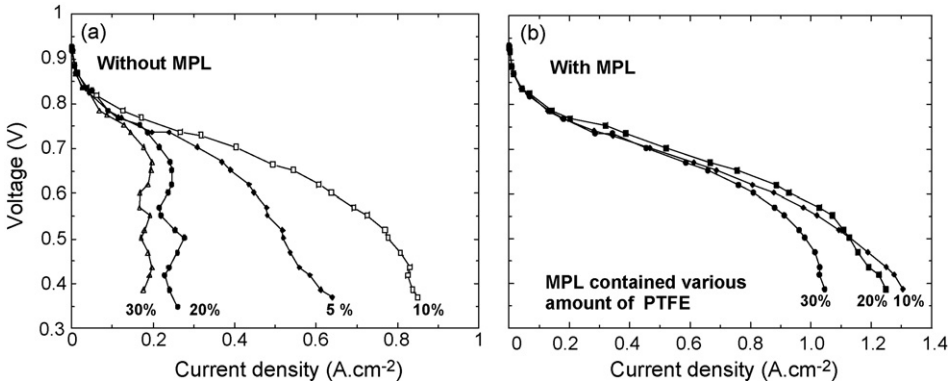

Fig. 9. (a) GDL without MPL, MEA performance at different PTFE loading in the GDL, (b) GDL with MPL, MEA performance at different PTFE loading in the MPL. Testing conditions are following: cell temperature 65 °C, H_2/O_2, humidification temperature at 80/70 °C, H_2/O_2 stoichiometry ratio at 1.5×/2×, and ambient pressure.

into the active area of the MEA, containment of the reactant gases in their respective compartments, conduction of the electric current and heat, and the structural integrity of the stack. Since the spaces between a pair of bipolar plates are the reaction chambers in the stack, the plates are in contact with highly reactive species, such as hydrogen peroxide and others, in an acidic environment. Corrosion resistance is very important requirement. They also should have higher volume utility and lower density. Thus the basic properties of the bipolar plate include high-electric conductivity, hermeticity, chemical corrosion-resistance, refraction, high-mechanical strength, low-surface roughness and lightweight.

Conventional bipolar plates are made of dense graphite or carbon composite or metal. Dense graphite material is more preferably used in PEMFC due to its low-electrical resistance. However, the use of dense graphite as the bipolar plate has many disadvantages. It has porous structure and warrants a post-filling process, which is time consuming and costly. Its flow channels need to be individual machined which adds to the cost moreover. The productions of dense graphite plates are expensive and time consuming. Considering the above drawbacks of dense graphite bipolar plates, composite bipolar plates have many advantages. The properties of the composite bipolar plates can be easily controlled by changing the material composition. The preferred bipolar plates shall be easily manufactured under various specifications, and mass production with low-raw material and process costs [27]. Cheap raw materials should be used, they are hermetic, so post-filling process is not required and the flow channels could be formed in the molding process itself [28]. Moreover, the composite bipolar plates will have better flexural strength then the dense graphite material. These benefits of using composite material lead us to the development of composite bipolar plates.

In order to improve the flexural strength, a copolymer of high-molecular weight rubber and vinyl ester are used as the molding material [29]. About 20–40 wt.% of block copolymer and 60–80% of conductive carbon fillers were added to a dispersing solvent. Other additives such as rheology modifiers and de-molding agents were also added. The mixture was stirred with a high-speed stirrer for 20–30 min. Attention must be given to avoid the loss of solvent during the stirring process. After stirring, the mixture was charged into the bulk molding compound kneader (BMC kneader), and kneaded by masticator vanes for 30–40 min. Before hot embossing, the mold was heated to 140–190 °C. The kneaded mixture was then appropriately weighted and charged into cavities of the mold. The mold was pressurized to 100–150 kg cm^{-2} over 5–10 min to harden the kneaded mixture. After de-molding by an automatic de-molding system, the composite plate was placed in an oven at 140–190 °C for 24 h to ensure complete hardening.

The flexural and tensile strengths of the bipolar plates are in Fig. 10a and b. Fig. 11 is the finished composite bipolar plates.

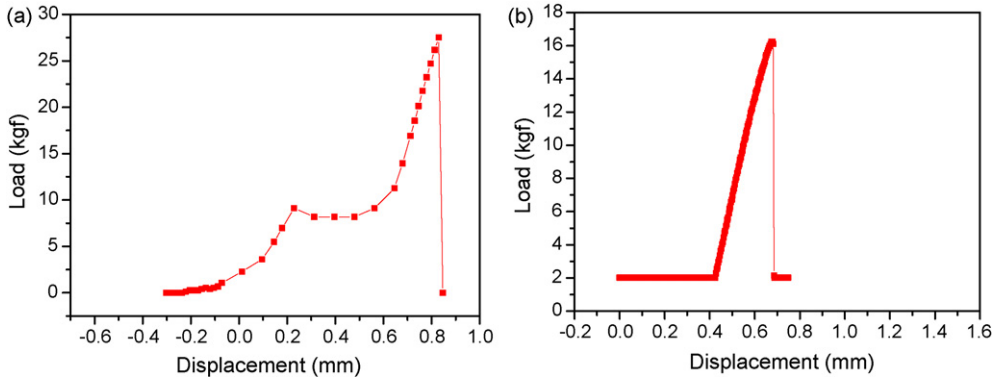

Fig. 10. (a) Flexural strength of rubber reinforced vinyl ester composite bipolar plate and (b) tensile strength of rubber reinforced vinyl ester composite bipolar plate.

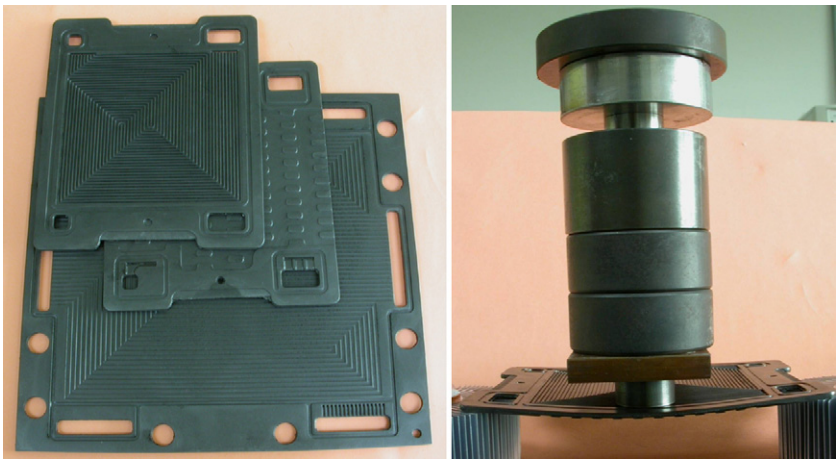

Fig. 11. Composite bi-polar plate.

Material properties of these composite plates are in Table 2. The material property requirements for bipolar plates set by U.S. DOE are also listed in Table 2 for reference. The present composite plate has two significant advantages over the conventional graphite plate. First, they are low-cost. The cost of the composite plate is about only 10% of the graphite plate, which needs CNC machining of flow channels. Second, the production time of a stack (turnaround time of a stack design) with composite plates can now be completed in 2 weeks maximum as compared to about 3 months using the graphite plate. The gain in the stack design turnaround time is most precious at this stage of development.

3.3.4. Structure analysis of a fuel-cell stack

A PEM fuel-cell stack has a series of repeating cell-units. The cell-units are assembled together between a pair of metal endplates and the entire assembly is compressed through several threaded tie-bolts with nuts on either end. The clamping force of PEM fuel cell must be sufficient to seal the stack assembly without gas leakage and to reduce the contact resistance. The damage to fuel cell components due to non-uniform distribution of assembly pressure should be avoided. In order to achieve a better and uniform pressure distribution many stack design concepts have been proposed [30–32].

We have used finite element analysis (FEA) method to study the pressure distribution in our fuel-cell stack assembly. As a result, the conventional fuel-cell stack design was modified to improve the assembly pressure distribution. To verify the performance of the new stack design, FEA method was used to compute the structural responses of the fuel-cell stack through the ANSYS software. This FEA procedure was written into a parametric analysis program using the ANSYS parametric design language (APDL). The safety of the stack components can be guaranteed and better pressure distributions over the stack areas can be obtained through comparing the FEA results. The analysis procedure is shown as in Fig. 12. The simplified solid model was exported to ANSYS for establishing the finite element model. Two types of element, including 3D high-order elastic solid element and non-linear contact plane element were used to mesh the solid model. The material properties of each component are assumed linear and elastic. The material properties of each component are listed in Table 3.

In order to make the design and verification procedure more effective, the simulation model of the developed stack is simplified to a 1/8 model according to approximate geometrical symmetry. The assembly pressure is generated through 12 tie-bolts. Each tie-bolt generates 217 kgf tightening force

Table 2
Property of composite bipolar plate

Properties	DOE	ITRI
Tensile strength (MPa)	20.7	23.8
Flexural strength (MPa)	27.6	42.1
Refraction (°C)	–	200
Conductivity (S cm^{-1})	100	150
Corrosion resistance in HCl of pH 0 (μA cm^{-2})	<16	<1
Density	–	1.57

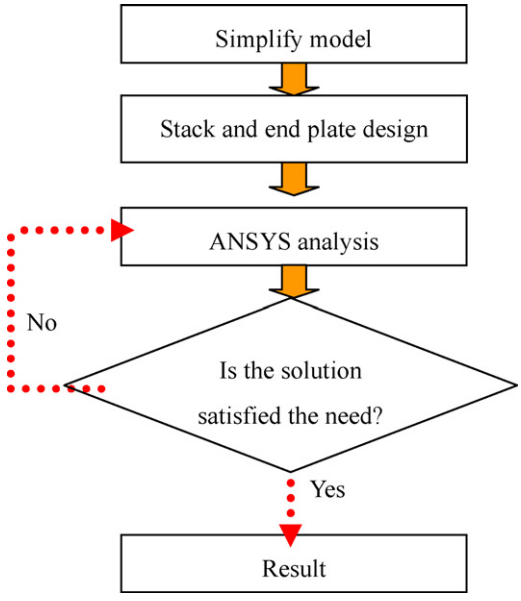

Fig. 12. The analysis procedure of FEM.

Table 3
Material properties of fuel-cell components

Component name	Material name	Young's modulus (kgf mm^{-2})	Yield stress (kgf mm^{-2})	Poisson's ratio
End plate	Al-Alloy-075-T6	7,340	47	0.33
Bolt and nut	Stainless steel-316	21,080	30	0.29
Carbon plate	Carbon	1125.4	4.077	0.33
MEA	NA	1223.2	NA	0.33
Gasket and o-ring	Silicone–rubber	225.3	NA	0.33
Collector	Copper	12,244	20.38	0.34

for the experiments. The FEA analysis results of various sub-components are shown in Fig. 13a–d. Since the tightening force is applied on the skirts of the endplate, stress is lager at the skirts and it drops considerable toward the center creating a non-uniform distribution. The circuit stress distribution is displayed around the endplate as shown in Fig. 13b. Consequently, the largest Z-dir. displacements appear on the tie-bolt holes of end-plate in Fig. 13c. Fig. 13d shows the von-Mises stress distribution of the contacting plane between the endplate and its neighboring cell-unit. It reveals that this stack design has a circular stress distribution to prevent gas leakage from the manifold.

In an effort to reduce the weight and volume of the stack, the thickness of the end plate was reduced by half and the same analysis was performed for the modified design. The results of the analysis are shown in Fig. 14. The stress distribution is not continuous at the corners and is weak on the top and bottom of Fig. 14a. To improve these conditions, the bolt and nut positions were modified, respectively, as those shown in Fig. 14a. Fig. 14b shows the von-Mises stress distribution of the contacting plane between the endplate and its neighboring cell-unit after modification. Compared with the original design, Fig. 14a, the stress distribution is no longer discontinuous and it also increases on the bottom and top of the end plate. Table 4 shows the effect of stress and displacement of each stack component before and after modification. It indicates that it is possible, by modifying the bolt and nut holes positions on the end plate, to smoothen the von-Mises stress to avoid the stress concentration and to improve the reliability of the stack.

3.3.5. Flow channels simulation

Many single cells are compacted closely in a fuel-cell stack and hence there is a possibility of uneven flow distribution of reactant gases across the stack [33–35]. Pressure variation and flow distribution in the stack were studied using computational fluid dynamics (CFD). The model is a two-dimensional stack composed of 72 cells filled with porous media. Two models as shown in Fig. 15a and b are constructed to evaluate pressure drop caused by channel flow resistance. The manifold width is

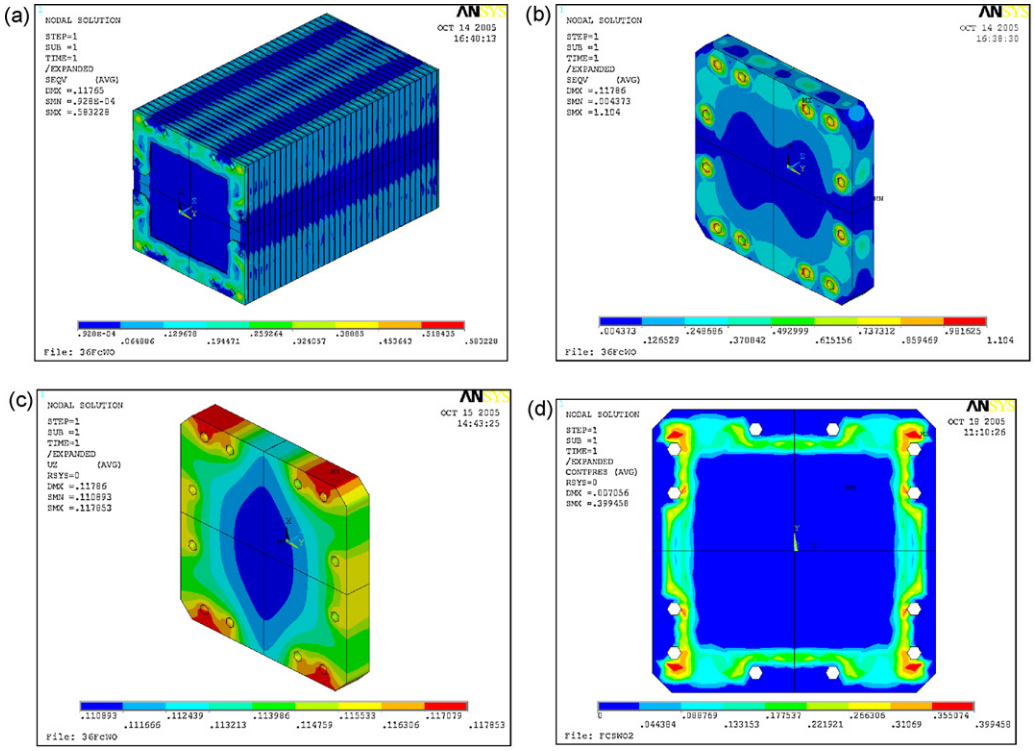

Fig. 13. Results from structural analysis. (a) The von-Mises stress distribution of bipolar plates, (b) the von-Mises stress distribution of the endplate (30 mm thick), (c) Z-dir. displacement of endplate and (d) the von-Mises stress distribution of the contacting plane between the endplate and its neighboring cell-unit.

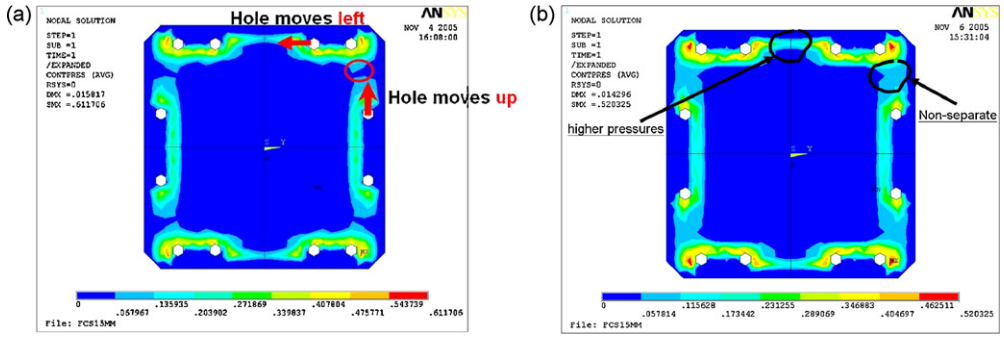

Fig. 14. (a) The von-Mises stress distribution of the contacting plane between the endplate (15 mm thick) and its neighboring cell-unit and (b) the von-Mises stress distribution of the contacting plane between the endplate and its neighboring cell-unit after modifying the positions of bolt and nut holes as indicated in (a).

Table 4
The simulation result before and after modification

	Max. von-Mises stress (kgf mm^{-2})			Max. deformation (mm)		
	Original	Modified	Variation (%)	Original	Modified	Variation (%)
Endplate	1.558	1.355	13	0.016461	0.014776	10.2
Carbon-plates	0.760828	0.747149	1.8	0.02212	0.01411	36.2
Collector	1.275	1.233	3.3	0.033045	0.019670	40
MEA	0.8975	0.772907	13	0.006959	0.006216	10.5

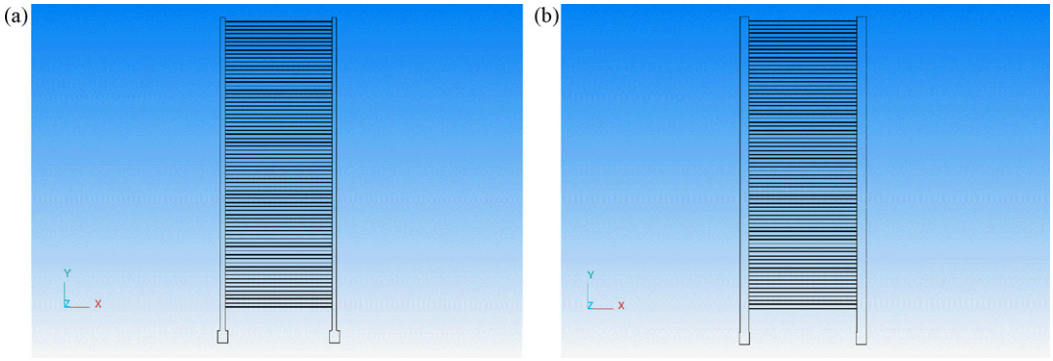

Fig. 15. Schematic of fuel cell stacks with different manifold width.

6 mm for Fig. 15a and is 12 mm for Fig. 15b. In order to simplify this model, electrochemical reactions, heat and mass transport phenomena are ignored and air is treated as working fluid to investigate flow distribution in stacks. Design parameters and modeling conditions are given in Table 5.

In the mathematical model, continuity, momentum, turbulent kinetic and turbulent dissipation rate equations are solved until the iterative process meets the convergence criteria. In order to simulate turbulent flow, the standard κ–ε model was employed to deal with related transport equations. ESI-CFDRC software is used to conduct the computation. Design parameters such as the permeability of porous media and manifold width are used to study their effects in each case and to estimate the degree of uniformity of the flow distribution. The cases analyzed are shown as follows:

Case 1: permeability $\kappa = 2.5 \times 10^{-10}$, manifold width $D = 6$ mm.

Table 5
Stack model parameters and modeling conditions

Variable	Value	Variable	Value
Number of cells	72	Gas permeability in cell channel (m^2)	2.5×10^{-10} and 2.5×10^{-9}
Gas channel depth (mm)	0.8	Back pressure (kPa)	101
Cell-to-cell distance in manifold axis (mm)	6	Air flow rate (SLPM)	300
Manifold width (mm)	6 and 12	Air viscosity (kg m^{-1} s^{-1})	1.846×10^{-5}
Width of inlet and outlet holes (mm)	15	Air density (kg m^{-3})	1.1614
Porosity in cell channel	0.4		

Case 2: permeability $\kappa = 2.5 \times 10^{-10}$, manifold width $D = 12$ mm.
Case 3: permeability $\kappa = 2.5 \times 10^{-9}$, manifold width $D = 6$ mm.
Case 4: permeability $\kappa = 2.5 \times 10^{-9}$, manifold width $D = 12$ mm.

By changing permeability, the influence of channel flow resistance on flow distribution can be investigated. Generally, for most channel patterns, the pressure drop is on the order of 10^0 to 10^1 kPa. There is one order of magnitude difference in permeability for cases analyzed so one can also expect approximately one order of magnitude difference in the overall pressure drop for the cases with the same manifold width. This is indeed the case, as demonstrated by the results shown in Fig. 16a and b. The results are for the cases 2 and 4 with the manifold width of 12 mm. The dimensionless cell pressure distribution and mass flow rate are shown in Fig. 16c and d, respectively.

In gas-distribution processes, pressure drops in channels drive gases into each cell from manifold and pressure drops are dominated by channel and manifold design. Comparing Fig. 16c and d, one confirms the correlations between cell pressure drops and flow distribution, i.e. a larger cell pressure drop causing higher cell feeding rate. Channels with large flow resistance contribute to more pressure drop, and then cause a more uniform flow distribution. Therefore, channel design with large flow resistance is advantageous for flow distribution. While manifold widths increase, a more uniform flow distribution will also be achieved. Therefore, the manifold in stacks should be as large as possible, and, for a given flow rate, this can also lower the overall stack pressure drop. The trends for stack design are focused on low-pressure drop and high performance. However, conflicts always exist between the two. A larger manifold size, when practical, is an option to optimize the fuel-cell stack design for flow uniformity and low-pressure drop.

3.3.6. Stack assembly

The fuel-cell stack had 72 single cells assembled in series. Brief details about each component are described in this section. Schunk composite bipolar plates of dimension 220 mm × 220 mm × 3 mm were used. O-rings were placed on the periphery of water flow channels. Both sides of MEA were sealed with silicon rubber gaskets. An o-ring was placed on the periphery of the hydrogen flow channel to ensure gas tight sealing. End plates were aluminum alloy with dimensions of 220 mm × 220 mm × 30 mm. Gold-plated current collectors were placed between the end plate and stack. The MEA and carbon cloth were purchased from a MEA vendor with an active area of 16 cm × 16 cm. The anode catalyst was Pt alloy of 0.45 mg cm^{-2} and the cathode catalyst Pt of 0.6 mg cm^{-2}.

During the stack assembly, two positioning rods were used for the alignment. The end plate, bipolar plate, sealing gasket, MEA, etc. were aligned and stacked one by one. Twelve M10 bolts were used to compress the stack to the point that bipolar plates were firmly in place. The stack was then transferred to an assembly station where it was compressed until the distance between each cell was around 0.5 mm. The bolts were tightened with a torque of 120 kgf cm.

After the assembly, the stack was filled with nitrogen for half an hour to detect any possible leakage. Then, the stack was activated by passing through the reactant gases. During the activation process, flows of hydrogen and air were kept at 1.5 and 2.0 stoichiometry, respectively. The reactant gases were humidified

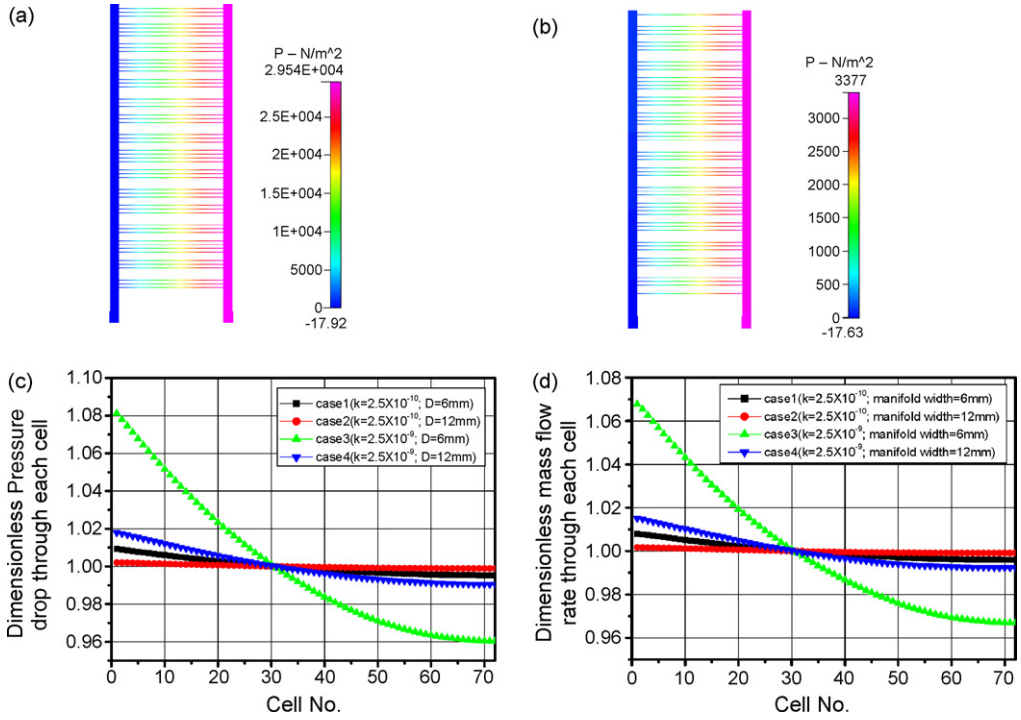

Fig. 16. Stack flow pressure distribution and dimensionless pressure drop and feed rate. (a) Pressure distribution of case 2, (b) pressure distribution of case 4, (c) dimensionless cell pressure drop for each case and (d) dimensionless cell mass flow rate for each case.

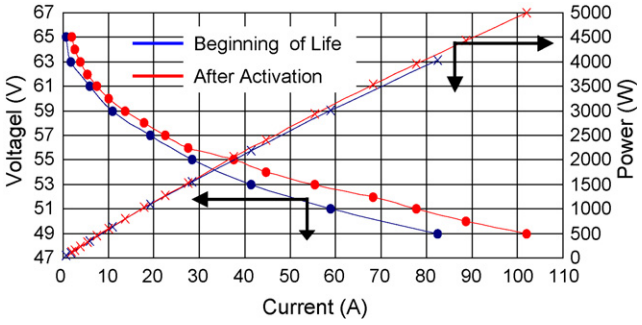

Fig. 17. *I–V* curve of the fuel cell stack.

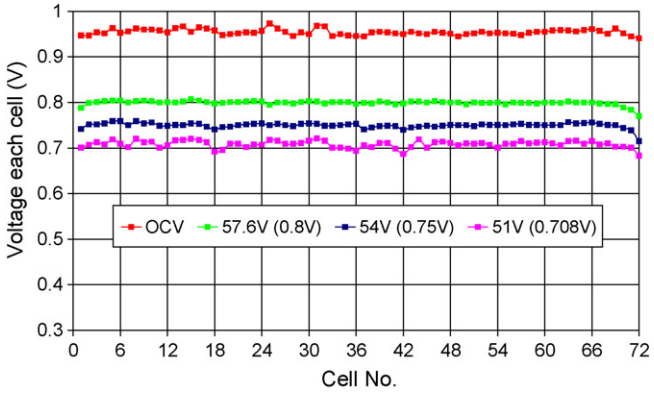

Fig. 18. Voltage distribution of individual cells of the stack.

at 60 °C at ambient pressure. Voltage of each cell was monitored during the activation procedure. The *I–V* curve was obtained by a 5 kW test station under voltage scanning mode. The open circuit voltage (OCV) was around 68 V. Test results at various loads are given in Fig. 17.

The stack performance was gradually improved through the activation process. The design point of the stack was 64 A at 50 V. Output current reached 70 A at the beginning of activation and reached 88 A after activation. The current density was 0.346 A cm^{-2}, and the power density was 0.24 W cm^{-2}. The maximum output power measured was 5 kW, limited by the capacity of the test station for this instance. The voltage distribution of individual cells was measured at open circuit and loads. The flow rates of hydrogen and air were 20 SLPM (standard liter per minute, 1.5 stoichiometry) and 80 SLPM (2.0 stoichiometry), respectively. Both gases were humidified at 65 °C and the temperature of cooling water was kept at 55 °C. Test results are given in Fig. 18. The voltage distribution was relatively uniform across the entire stack. The voltage of the last few cells is slightly lower than the rest. This might be due to the U-shape manifold design of the stack.

3.4. System integration

Fig. 19 shows snap shots of this integrated PEMFC CHP system. Water tank is separate from the chase. The system is capable of using either hydrogen or NG as its fuel. The flow diagram of this system was given in Fig. 1. The start-up behavior of this system is reported below.

The system was operated at constant current mode at 19.5 A, which is equivalent to the MEA current density of 76 mA cm^{-2}. The air was slightly pressurized to 35 kPa with an air compressor and, then, it is humidified with a shell-tube type humidifier. Prior entering the stack cathode, it passed through a water separator to remove entrained liquid water. This system has two water circulating loops to isolate possible contamination to the stack. The inner loop removed the heat from the stack and the outer loop warmed up the water in the hot water tank. It dumped excessive heat via a radiator. Cooling water in the inner loop is circulating through the stack at flow rate of 2.6–2.8 L min^{-1}. A brazed plate heat exchanger transferred the heat absorbed by the inner loop to the hot water tank via the outer loop. Water circulation rate of the outer loop is 6.6 L min^{-1}.

For operation with hydrogen fuel, the air and hydrogen flow rate were about 140 and 10 L min^{-1}, respectively. Fig. 20 is a plot of the dynamics of stack voltage, temperatures of inlet/outlet hydrogen, air, and cooling water. The cell voltage raised to a maximum value of 54.2 V in 30 min, then it gradually fell to a near steady-state value of 52.2 V. The stack output power was 1 kW (52 V × 19.5 A). For a stack with 72 cells, this corresponds to an average cell voltage of 0.73 V and voltage conversion efficiency of 59% (0.73/1.23 V). It took about 2 h for the system

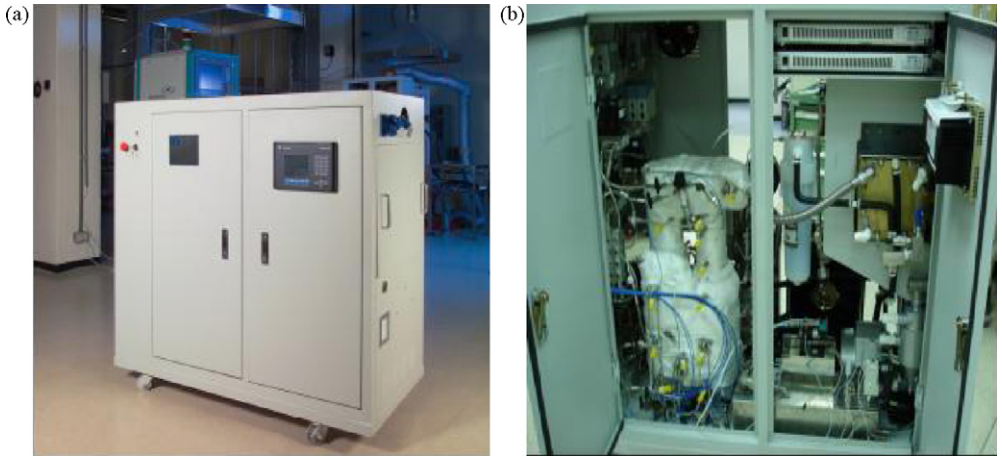

Fig. 19. The small PEMFC CHP prototype system. (a) The system without the water tank and (b) front inside view of the generator unit.

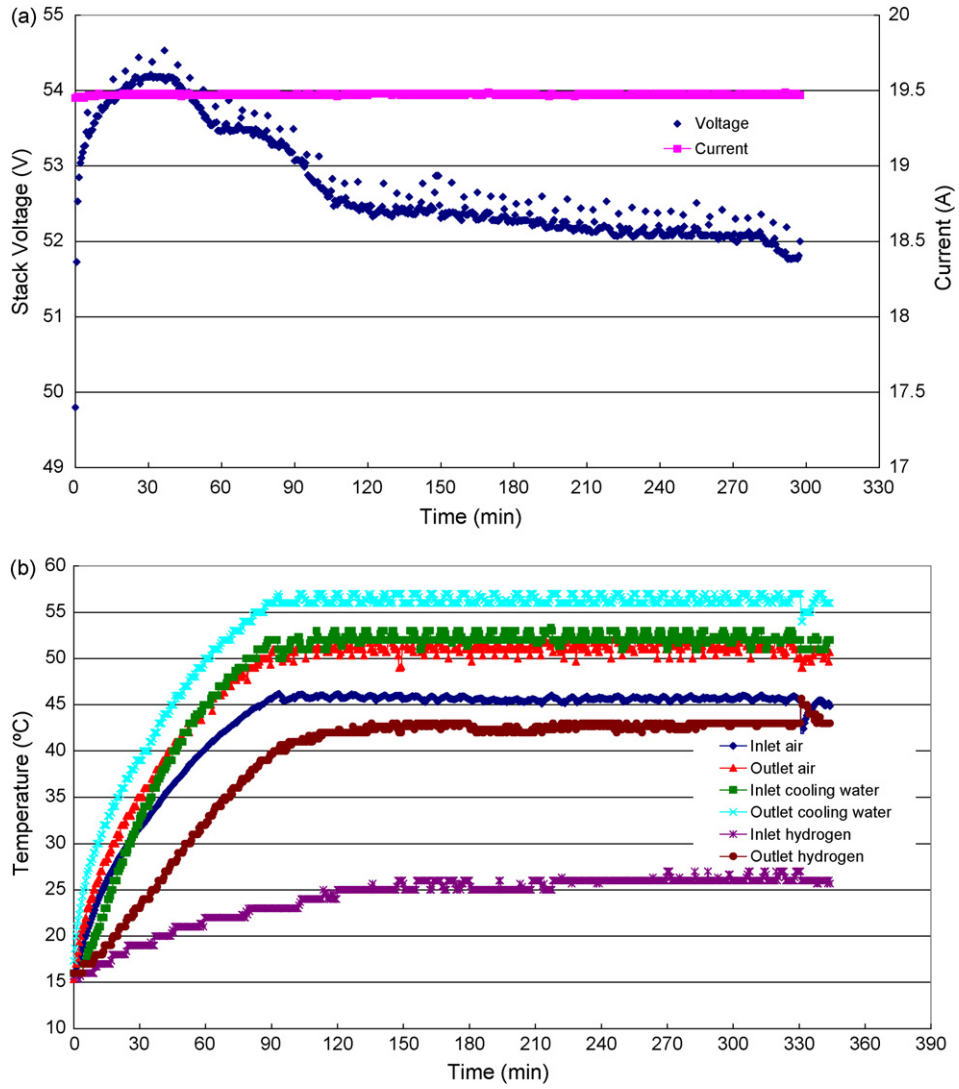

Fig. 20. Characteristics of the prototype PEMFC CHP system start-up with hydrogen feed. Plot of (a) stack voltage and current and (b) temperatures of outlet/inlet cooling water, air, and hydrogen.

temperature to reach its steady state. The difference of cooling water temperature between the outlet and inlet is 4 °C. With a flow rate of 2.8 L min^{-1}, the heat removal rate from the stack was around 0.8 kW. The hydrogen was fed into the stack without pre-heating. The inlet hydrogen temperature was gradually raised from 15 °C to a steady-state value of 26 °C because heat from the stack was conducted to the measuring station.

For operation with NG fuel, Fig. 21 is a plot of the dynamics of stack voltage, temperatures of inlet/outlet hydrogen, air, and cooling water. The cell voltage raised to a maximum value of 53 V in 30 min and, then, it gradually fell to a near steady-state value of 48.3 V. The stack output power was 0.93 kW (48.3 V × 19.5 A). The cell voltage and power output of the system with NG fuel is lower than the system with hydrogen fuel (52 V vs. 48 V and 1 kW vs. 0.93 kW). This is partially due to the low-hydrogen concentration in the reformate gas (<45% H_2). However, the system temperature with NG fuel reached steady state within 1 h. This is because the reformate gas at the inlet of the stack was kept at 65 °C. The warm reformate gas helped the system reach its steady state faster (1 h vs. 2 h for non-preheated pure hydrogen fuel). However, the heat carried by the reformate gas needed to be removed along with the heat generated by the stack when the system reached its steady state. With cooling water flow rate of 2.8 L min^{-1}, about 1.4 kW of heat was removed by the cooling water (0.8 kW for non-preheated pure hydrogen fuel).

Although the test run continues, a few conclusions can be made from the preliminary tests. The electrical energy conversion efficiency of the entire system is about 28%. This indicates consumption by the BOP was excessive and needs to be investigated further. The overall energy conversion efficiency (electricity + heat recovery) is greater than 60%. The system with NG fuel started up faster than the system with pure hydrogen fuel, discounting the start-up time required by the reformer. However, the control of the NG system is more complicated than the hydrogen system. The heat rejection rate of the NG system is much higher than that of the hydrogen system. The power output of the NG system is slightly lower than that of

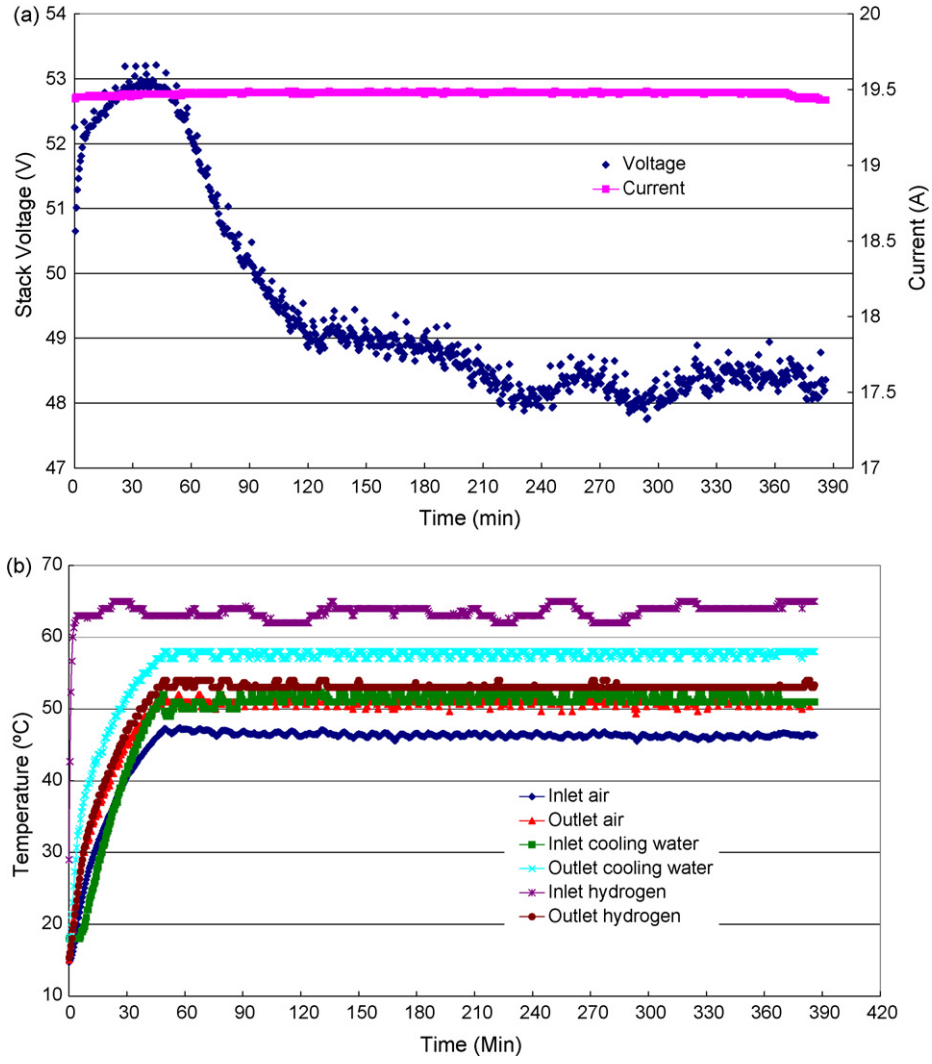

Fig. 21. Characteristics of the prototype PEMFC CHP system start-up with NG feed. Plot of (a) stack voltage and current and (b) temperatures of outlet/inlet cooling water, air, and hydrogen.

the hydrogen system. For a PEMFC CHP system, it can be said the hydrogen system is more suitable for high electricity-to-heat applications and that the NG system is more appropriate for high heat-to-electricity applications.

4. Conclusion

The research and development of a small PEMFC combined heat and power system was discussed in details. The test run of the prototype system is on going to validate the system integration design and for future development to investigate key component specifications based on system durability (reliability and life) and cost. The electrical and thermal efficiency of the current prototype system, as run, is still with much room for improvement. Moreover, components interact with each other and their best specifications heavily depend on each other, as was the case between the air blower and the fuel-cell stack. This can only be realized through system integration. The steady-state operation of the reformer at the nominal condition is satisfactory but its control algorithm and technology will need to be simplified and robust for more practical operations. It was also found that component manufacturability, as manifested by bipolar plates, plays a critical role in the acceleration of PEMFC technology development and cost reduction.

Acknowledgements

The authors would like to express their appreciation of the support for this work from the Petroleum Fund, under the auspices of the Bureau of Energy, Ministry of Economic Affairs, ROC. The authors would also like to acknowledge the following staff members for their contributions during the preparation of this paper: Mr. Roger Chang, Mr. Lung-Yu Sung, Mr. Andrew Chou, Mr. Shiqah-Ping Jung, Mr. Ssu-Tai Lin and Mr. Jeff Yeh, and the Department of Mechanics Engineering of National Taiwan University for collaboration on the stack structural analysis. Special thanks to Dr. Palanichamy Krishnan for his valuable comments.

References

[1] K. Kordesch, G. Simader, Fuel Cell and Their Applications, VCH Publishers, New York, 1996.
[2] J. Larminie, A. Dicks, Fuel Cell Systems, Wiley, New York, 2000.
[3] M. Bischoff, J. Power Sources 154 (2006) 461–466.
[4] S. Geiger, M. Cropper, Fuel Cell Today: Fuel Cell Market Surv. (2003).
[5] K. Adamson, A. Baker, D. Jollie, Fuel Cell Today: Fuel Cell Sys. (2004).
[6] W. Vielstich, A. Lamm, H. Gasteiger, Handbook of Fuel Cells, vol. 3, Wiley, New York, 2003, Part 3.
[7] J.H. Hirschenhofer, D.B. Stauffer, R.R. Engleman, M.G. Klett, Fuel Cell Handbook, 4th Ed., Parsons Corporation, Pennsylvania, for the U.S. Department of Energy, 1998.
[8] W. Colella, J. Power Sources 106 (2002) 388–396.
[9] G. Gigliucci, L. Petruzzi, E. Cerelli, A. Garzisi, A.L. Mendola, J. Power Sources 131 (2004) 62–68.
[10] C.-E. Hubert, P. Achard, R. Metkemeijer, J. Power Sources 156 (2006) 64–70.
[11] New Energy Foundation of Japan, Stationary Fuel Cell Demonstration Project, presented at the 4th Steering Committee Meeting of IPHE, September 2005.
[12] Research Institute for Energy Economy on behalf of the Federal Ministry of Economics and Labour, Germany, Strategy Report on the Research Needs in the Field of Hydrogen Energy Technology, 2005, pp. 32–34.
[13] J.M. Zalc, D.G. Lffler, J. Power Sources 111 (2002) 58–64.
[14] A. Igarashi, S. Urawa-Shi, H. Higashi, M. Mizobuchi, N. Hashimoto, K. Kinugawa, European Patent 1,161,991 (2001).
[15] T. Hirabayashi, European Patent 1,184,445 (2001).
[16] Q. Okada, M. Echigo, WO Patent 01/78892 (2001).
[17] C. Liu, A. Johnson, J.-S. Lai, IEEE Trans. Ind. Appl. 41 (6) (2005) 1691–1697.
[18] R.-S. Lai, K.D.T. Ngo, IEEE Trans. Power Electron. 10 (3) (1995) 326–332.
[19] J. Kim, S.M. Lee, S. Srinivasan, C.E. Chamberlin, J. Electrochem. Soc. 142 (1995) 2670–2674.
[20] G. Squadrito, G. Maggio, E. Passalacqua, F. Lufrano, A. Patti, J. Appl. Electrochem. 29 (1999) 1449–1455.
[21] D. Chu, R. Jiang, J. Power Sources 80 (1999) 226–234.
[22] K. Scott, P. Argyropoulos, K. Sundmacher, J. Electroanal. Chem. 477 (1999) 97–110.
[23] P. Argyropoulos, K. Scott, A.K. Shukla, C. Jackson, Fuel Cells 2 (2002) 78–82.
[24] C. Lim, C.Y. Wang, Electrochim. Acta 49 (2004) 4149–4156.
[25] Z. Qi, A. Kaufman, J. Power Sources 109 (2002) 38–46.
[26] U. Pasaogullari, C.Y. Wang, J. Electrochem. Soc. 151 (3) (2004) A399–A406.
[27] V. Mehta, J.S. Cooper, J. Power Sources 114 (2003) 32–53.
[28] I. Hermann, T. Chaudhuri, P. Spagnol, Int. J. Hydrogen Energy 30 (2005) 1297–1302.
[29] E. Dreerman, M. Narkis, A. Sigmann, J. Appl. Poly. Sci. 72 (1999) 647–657.
[30] X. Wang, Y. Song, B. Zhang, Presentation at First International Conference on Fuel Cell Development and Deployment, 2004.
[31] B. Wozniczka et al., US Patent 5,993,987 (1999).
[32] Stephen A. Grot, US Patent 6,428,921 (2002).
[33] J.H. Koh, H.K. Seo, C.G. Lee, Y.S. Yoo, H.C. Lim, J. Power Sources 115 (2003) 54–65.
[34] G. Karimi, J.J. Baschuk, X. Li, J. Power Sources 147 (2005) 162–177.
[35] M.H.J. Pedras, M.J.S. de Lemos, Int. J. Heat Mass Transf. 44 (2001) 1081–1093.